Cold filamentary intensification and oceanic surface convergence lines

J. C. Mcwilliams, François Colas, M. J. Molemaker

Cold filamentary intensification and oceanic surface convergence lines

J. C. McWilliams,[1] F. Colas,[1] and M. J. Molemaker[1]

Received 3 June 2009; revised 8 July 2009; accepted 28 July 2009; published 16 September 2009.

[1] The reflectance images of the oceanic surface are full of surfactant lines created by surface velocity convergences, with typical line spacings of 0.1–10 km, i.e., in the submesoscale range. Here we propose a dynamical explanation by the process of filamentary intensification that shrinks the transverse scale of rectilinear surface temperature extrema at a super-exponential rate by the action of horizontal deformation flows associated with mesoscale eddies. This process is analogous to deformation-induced frontogenesis with sharpening temperature gradients accelerated by its ageostrophic secondary circulation. In the particular case of cold filaments, the shrinking rate, surface convergence, and downwelling are especially strong because of the configuration of ageostrophic acceleration. This behavior is demonstrated theoretically with idealized two-dimensional solutions and illustrated in a realistic regional circulation simulation near Peru. **Citation:** McWilliams, J. C., F. Colas, and M. J. Molemaker (2009), Cold filamentary intensification and oceanic surface convergence lines, *Geophys. Res. Lett.*, *36*, L18602, doi:10.1029/2009GL039402.

1. Introduction

[2] Oceanic surface convergence lines are abundantly seen in sun glint and Synthetic Aperture Radar (SAR) reflectance images (Figure 1). Typical line separations are in the submesoscale range of 100 m–10 km. The visual indicator is a reduced amplitude for small-scale surface gravity waves caused by selective damping in places with high surfactant concentrations [*Espedal et al.*, 1998], laterally gathered through convergent surface flows and vertically trapped by being too buoyant to follow the downwelling velocity underneath. In these convergent, downwelling circulations, neutrally-buoyant dissolved materials are carried down into the oceanic interior, providing an important vertical conduit.

[3] Several dynamical mechanisms are known for generating rectilinear surface convergence patterns, including internal waves on the near-surface pycnocline (most conspicuously as solitons [*Zhao et al.*, 2004]) and wind-wave Langmuir circulations [*Leibovich*, 1983]. The first of these does not occur in very many places and is readily identified by its rapid pattern propagation. The second mechanism has a typical line-separation scale comparable to the boundary-layer depth, i.e., <100 m in most places. These mechanisms do not satisfactorily account for abundant convergence lines with apparently slow propagation and large lateral separation.

[4] Another convergence-line mechanism is surface fronts, whose abundance is high in the submesoscale regime at least in some regions [*Castelao et al.*, 2006]. The theory of frontogenesis is well-known from its atmospheric context [*Hoskins*, 1982]: favorably-aligned lateral density gradients rapidly sharpen in the presence of a larger-scale, horizontally-confluent deformation flow, and an ageostrophic secondary circulation cell around the frontal axis with surface convergence on the heavy side that accelerates the sharpening (Figure 2, left). The secondary circulation acts to restore cross-front geostrophic, hydrostatic balance against disruption by deformation. Frontogenesis is also relevant to the upper ocean [*Capet et al.*, 2008]. Here we propose a related mechanism, filamentary intensification, where a deformation flow acts on an isolated, favorably-aligned, heavy-density (e.g., cold) filament, causing rapid narrowing and a two-celled secondary circulation with even stronger surface convergence and downwelling at its center (Figure 2, right) than in frontogenesis. There is analogous light-density (hot) filamentary intensification, but its secondary circulation has central divergence and upwelling that retard the rate of narrowing.

[5] *Lapeyre and Klein* [2006] advocate the importance of surface filaments for vertical material flux, but they make a restrictive dynamical assumption (surface quasigeostrophy, SQG) that lacks the sharpening acceleration from secondary circulation and thus does not expose the full potency of cold filamentary intensification. *Hakim et al.* [2002] hypothesize the ageostrophic acceleration mechanism but do not provide a clean demonstration.

2. Upper-Ocean Response to a Deformation Flow

[6] We solve for the evolution of idealized flow configurations that illustrate frontogenesis and filamentary intensification, using the Boussinesq equations for a rotating, stably stratified, incompressible, inviscid fluid in which density is an adiabatic Lagrangian invariant. We assume a background deformation flow, $\mathbf{u}_d = (-\alpha x, \alpha y, 0)$, with a deformation rate $\alpha(t) \geq 0$ and uniform stratification with buoyancy frequency N (Figure 2). Cartesian coordinates are $\mathbf{x} = (x, y, z)$, with $\hat{\mathbf{z}}$ vertically upward, parallel to the rotation axis with rotation frequency $f/2$ and anti-parallel to the gravitational acceleration g. This flow has no vorticity, no horizontal divergence, and no associated density variation even in the presence of a background vertical stratification; however, it does have a spatially-uniform horizontal strain rate 2α. Lagrangian parcels follow trajectories ($X(t) = xe^{\beta}$, $Y(t) = ye^{-\beta}$, z), with $\beta = \int_0^t \alpha(t')\, dt'$, that are confluent toward the y axis. $\mathbf{u}_d$ is conducive to sharpening material gradients in the $\hat{\mathbf{x}}$ direction while weakening them in $\hat{\mathbf{y}}$. We take a local viewpoint that $\mathbf{u}_d$ arises from "larger-scale" flow dynamics controlled remotely away from the frontogenetic region; its history is externally specified by $\alpha(t)$. For

[1]Institute of Geophysics and Planetary Physics, University of California, Los Angeles, California, USA.

0094-8276/09/2009GL039402

Figure 1. RADARSAT SAR image of the Santa Barbara Channel at 1400 UT on January 8, 2003. The area is 100 km by 110 km. The image was provided by B. Holt, Jet Propulsion Laboratory, and processed at the Alaska Satellite Facility. (Copyright by the Canadian Space Agency (2003)).

example, a time-varying vorticity field with compact support and finite circulation has a far-field velocity that is dominated by strain and can be locally Taylor-expanded around the frontal location, $(x, y, z) = 0$, as a dynamically inconsequential uniform velocity plus the deformation flow $\mathbf{u}_d$ plus higher-order spatial-polynomial components.

[7] Now consider the evolution of a localized flow perturbation $\mathbf{u} = (u, v, w)$, and its associated normalized pressure fluctuation $\varphi = p/\rho_0$ and buoyancy field $b = g(1 - \rho/\rho_0)$ in the presence of $\mathbf{u}_d$. ρ is the density field, and ρ_0 is its mean value. To focus attention on the sharpening x gradients, we assume for simplicity that the local flow perturbation is initially invariant in y; if so it will remain so for all time if we neglect possible three-dimensional instabilities. We transform the two-dimensional Boussinesq equations from (x, z, t) to $(X, Z = ze^{\beta}, t)$, anticipating that frontogenesis and filamentary intensification will often sharpen gradients in z as well as x: $D[u] - fv + e^{\beta}\partial_X\varphi = \alpha u$; $D[v] + fu = -\alpha v$; $D[w] - b + e^{\beta}\partial_Z\varphi = 0$; & $D[b] = 0$; $\partial_X u + \partial_Z w = 0$. $D = \partial_t + u\partial_X + (w + \alpha Z)\partial_Z$ is the material derivative in (X, Z, t) where the advection by $\mathbf{u}_d$ is implicit [*McWilliams et al.*, 2009]. We decompose b into its horizontal average $\langle b \rangle$ (Z, t) and deviation $b'(\mathbf{X}, t)$, with $\langle b \rangle$ $(z, 0) = N^2 z$.

[8] We choose initial conditions with a surface-intensified $b'(x, z, 0)$; a $v(x, z, 0)$ in hydrostatic, geostrophic balance $(f\partial_Z v = \partial_X b')$; and no ageostrophic secondary circulation $(u = w = 0)$. With $\alpha(0) = 0$, this is a stationary state. We specify $\alpha(t)$ as an increasing function that asymptotes to $\alpha_0 > 0$ and induces frontogenesis and filamentary intensification. (Its ramp-up over an interval of about $0.2\alpha_0^{-1}$ diminishes inertia-gravity wave excitation that would result from abrupt deformation.) Boundary conditions are $w = 0$ at the upper surface $Z = 0$ and vanishing perturbation velocity as $Z \to -\infty$ and $X \to \pm\infty$. The problems of interest are frontogenesis with initial $b'_{fro}(x, z) = v_0 f \ell_0 h_0^{-1} \exp[z/h_0]$ $erf[x/\ell_0]$ and filamentary intensification with $b'_{fil}(x, z) = b'_{fro}(x + d, z) - b'_{fro}(x - d, z)$ where $d = \pm 1.25\ell_0$ is chosen so that the filament has a single extremum in b' and approximately the same initial v and shear magnitudes as in the frontal initial condition (Figure 2). The sign of d determines the sign of the filamentary buoyancy perturbation; e.g., $d > 0$ is a positive (light, hot) anomaly. We choose parameter values relevant to submesoscale structures in subtropical oceans: $v_0 = 0.1$ ms^{-1}, $h_0 = 33$ m, $\ell_0 = 5$ km, $f = 10^{-4}$ s^{-1}, $N = 1.1 \times 10^{-2}$ s^{-1}, and $\alpha_0 = 10^{-6}$. The associated buoyancy scale is $b_0 = v_0 f \ell_0 / h_0 = 1.5 \times 10^{-3}$ m s^{-2} and temperature scale is $T_0 = b_0/Ag = 0.8$ C (for $A = -\partial_T \ln[\rho] \approx 2 \times 10^{-4}$ C^{-1}).

[9] A common but severe dynamical approximation is quasigeostrophy (QG), where $f\partial_Z v = \partial_X b'$ exactly and ageostrophic advection is neglected in D. A further approximation is surface QG (SQG), where additionally the interior QG potential vorticity is persistently zero $(q = \partial_X v + f\partial_Z b'/N^2 = 0)$. The SQG solution to our posed problem is very simple for both frontogenesis and filamentary intensification. The surface buoyancy perturbation is invariant in the transformed coordinates, $b'(X, 0, t) = b'(x, 0, 0)$, hence its x scale shrinks in time as $e^{-\beta}$, and its gradient $|\partial_x b'|$ increases as e^{β}. The interior $v(X, Z, t)$ and $b'(X, Z, t)$ are also

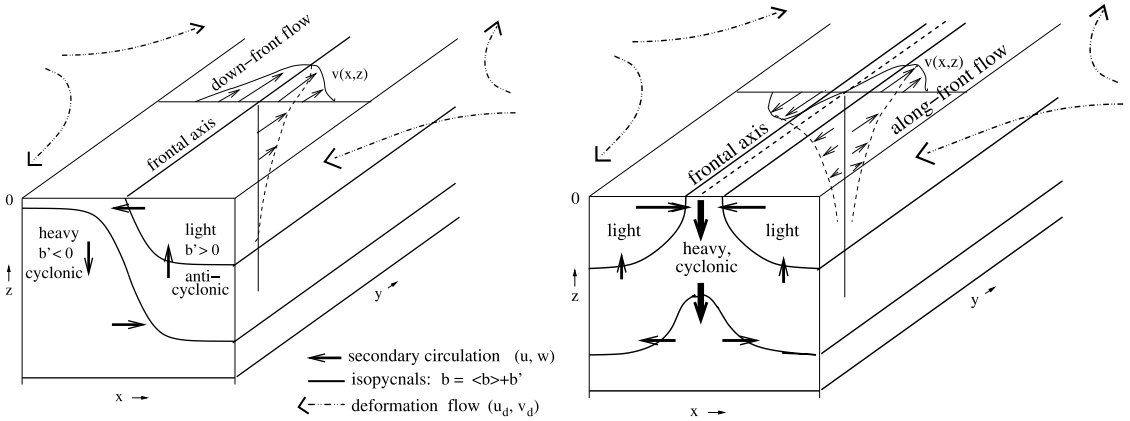

Figure 2. (left) Sketches of surface frontogenesis and (right) cold filamentary intensification ($d < 0$).

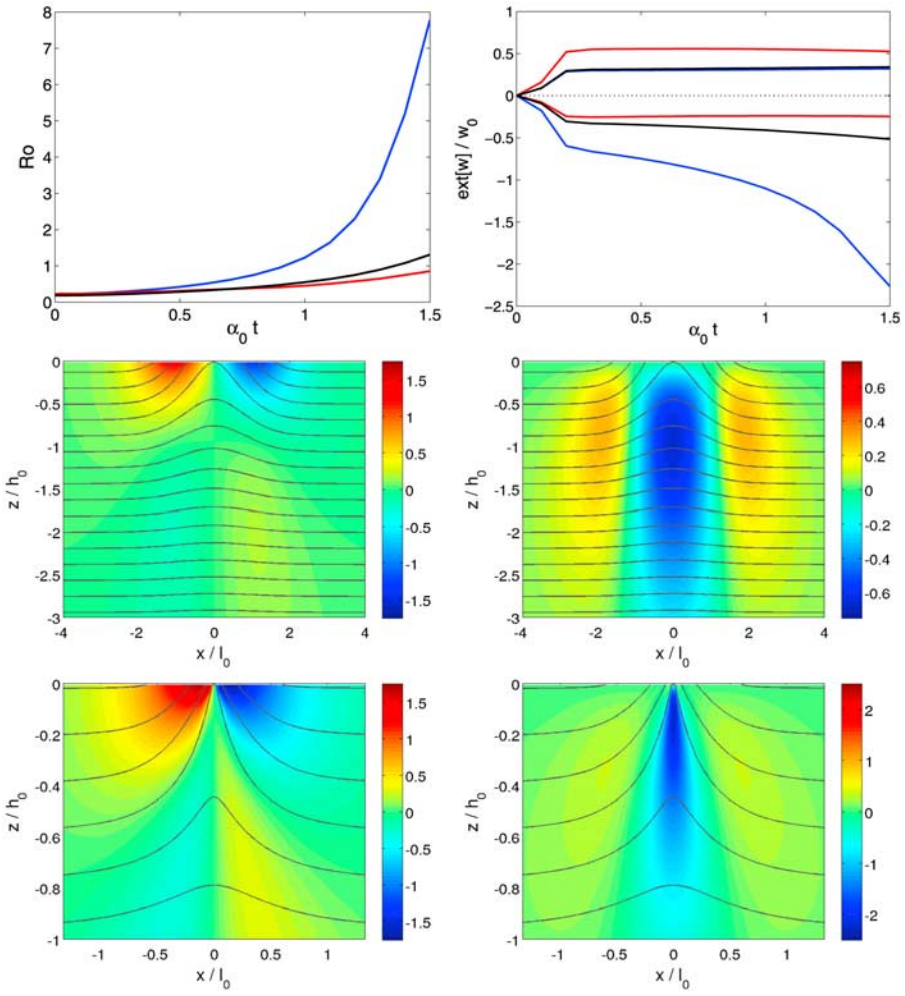

Figure 3. Responses to a deformation flow. (top left) $Ro(t)$ and (top right) $ext[w](t)/w_0$ for frontogenesis (black) and for cold (blue) and hot (red) filamentary intensification. Early increases in w are due to the ramp-up in $\alpha(t)$. Cross-sections for a cold filament at (middle) $\alpha_0 t = 0.3$ and (bottom) 1.5: u/u_0 and w/w_0 in color and b/b_0 with contour interval 0.5. At $\alpha_0 t = 1.5$, the plotted domain is smaller and w/w_0 amplitude range is larger.

time-invariant with exponentially shrinking x and z scales. There are secondary circulations as in Figure 2: frontogenesis has a single cell (with upward flow on the light side and an equal downward flow on the heavy side), and filamentary intensification has a double cell (with upward flow in the center for a hot filament or an equivalent central downward flow for a cold filament). The double cell is essentially a superposition of the single cells associated with the two opposite-signed fronts on either edge of the filament. Once the asymptotic value in $\alpha(t)$ is achieved, scale-estimated ageostrophic speeds are $u_0 = \alpha_0 v_0/f$ and $w_0 = \alpha_0 v_0 h_0/f\ell_0$, and they do not vary further in time. This SQG behavior is the basis for the argument by *Lapeyre and Klein* [2006] that fronts and filaments are important conduits for vertical material exchange.

[10] Qualitatively similar behaviors occur with Boussinseq dynamics (solved with the computational method of *McWilliams et al.* [2009]), but the true rates of frontogenesis and filamentary intensification are faster — i.e., super-exponential and sometimes even singular in finite time in the Semigeostrophic approximation [*Hoskins*, 1982] — because of advective acceleration by the ageostrophic secondary circulation. The secondary circulations are asymmetrical and stronger compared to SQG theory. This story is well-known for frontogenesis, and our solutions confirm the common understanding. Figure 3 (top) shows a spatially-extremal Rossby number $Ro(t) = \max[|\partial_x v|]/f$. It increases rapidly with time indicating the shrinking lateral scale and increasing shear, and it achieves values too large for consistency with geostrophic, hydrostatic balance (QG) after a time interval $\sim\alpha_0^{-1}$. Its growth rate here is super-exponential; e.g., by $t = 1.5\alpha_0^{-1}$, Ro has increased from its initial value by a factor of 2 more than e^{β}. Also shown are spatial extrema $ext[w](t)$ for the maximum and minimum w normalized by w_0. The downward w is much stronger than the upward w, and is associated with generation of stronger cyclonic vorticity ($\partial_x v/f > 0$) by vortex stretching on the heavy side. Vertical buoyancy flux $wb' > 0$ due to upward motion on the light side and downward motion on the heavy side, implying density restratification and generation of kinetic energy, as well as a cascade of available potential energy toward smaller scales by frontogenesis [*Capet et al.*, 2008].

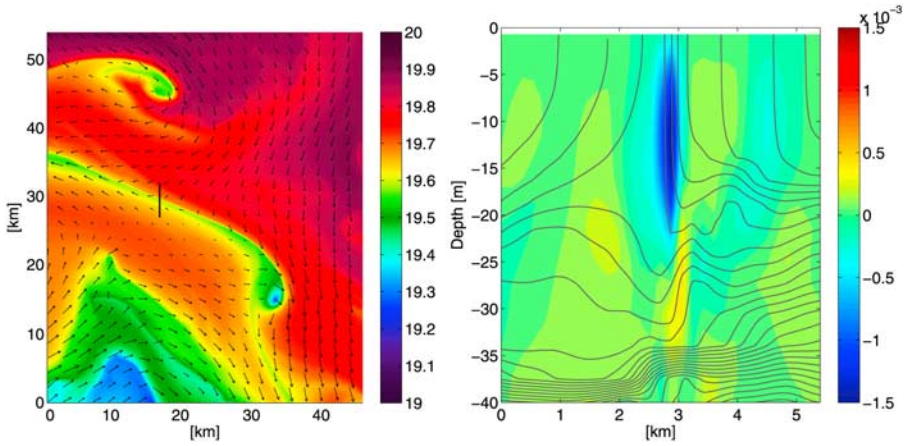

Figure 4. Snapshot in a subdomain of a realistic simulation off the coast of Peru: (left) surface $T(x, y, 0)$ [°C in color] and horizontal velocity [arrows, with a largest speed ≈0.25 m s^{-1}]; (right) vertical section (along the indicated black line in Figure 4, left) across the cold filament with w [m s^{-1} in color] and T [°C with gray contours and 0.025 °C spacing].

[11] The new story here is Boussinseq filamentary intensification. Analogous $Ro(t)$ and $ext[w](t)$ are in Figure 3 (top). From essentially similar initial values, the $Ro(t)$ show very different histories. For a hot filament, Ro increases modestly slower than for comparable frontogenesis, although it still attains $Ro \sim 1$ after $t \sim \alpha_0^{-1}$ and is increasing slightly faster than e^{β} by the end of the time interval shown. However, the intensification rate for a cold filament is dramatically larger than in either of the other two cases, with an increase by more than a factor of 8 times e^{β} by $t = 1.5\ \alpha_0^{-1}$. The central downwelling and its rate of increase are very much stronger in a cold filament. (Recall that SQG theory has sign-reversal symmetry for w between hot and cold filaments.) The explanation for the extra efficacy of cold filamentary intensification is reinforcement between the horizontal confluence by the deformation flow and the ageostrophic surface convergence above the central downwelling jet (rather than convergence laterally displaced from the confluence axis toward the dense side in a frontogenetic configuration). In hot filamentary intensification these two effects are opposing (albeit with confluence winning out in this example), making its sharpening rate even slower than in frontogenesis. As with frontogenesis, filamentary intensification causes restratification, kinetic energy generation by potential-energy conversion, and forward cascade of available potential energy. Thus, the theory for filamentary intensification is an extension of frontogenesis theory; i.e., a sharpening filament is a superposition of two adjacent and opposite sharpening fronts, exactly so in SQG and with a nonlinear modulation and acceleration in Boussinesq.

[12] Figures 3 (middle) and 3 (bottom) have cross-sections for (u, w) in cold filamentary intensification at an early time soon after the ramp-up in $\alpha(t)$ is completed and at a later time when the sharpening has substantially progressed. The late-time developments of very strong surface convergence and a central downwelling jet are evident, while the deep divergence and side upwelling velocities are relatively broader and weaker. Even at the earlier time, however, the overall pattern of the ageostrophic circulation is similar to its later form. The two-dimensional filamentary evolution, as in frontogenesis, will proceed to shrink its transverse scale and to increase its gradients without limit, as long as the deformation flow persists and no disruptive instability or turbulent mixing occurs.

3. Oceanic Filamentation and Filament Intensification

[13] Oceanic filaments are abundantly evident in satellite images of surface temperature and color in regions where strong lateral gradients occur (e.g., near boundary currents). The filamentation process that creates filaments is well known in two-dimensional and QG fluid dynamics. Material concentrations (including weak-amplitude potential vorticity anomalies) are approximately conserved following the horizontal flow, and their isolines are stretched into filaments in the regions of high strain between mesoscale eddies. This is the structural manifestation of the forward cascades of scalar variance and potential enstrophy. This type of passively-advected filament generation is readily simulated in oceanic general circulation models with mesoscale grid resolution (i.e., tens of km). However, when filamentary widths shrink into the submesoscale range (100 m – 10 km), the filamentary intensification process attains larger Ro with strong ageostrophic acceleration (section 2).

[14] A further demonstration of the occurrence of cold filamentary intensification comes from a realistic simulation of the regional circulation in the Southeastern Pacific [*Colas et al.*, 2008] using successive horizontal grid nesting refinements from the parent grid resolution of $dx = 7.5$ km to child grids with $dx = 2.2$, 0.5, and 0.18 km to expose submesoscale phenomena in the region offshore of Peruvian coastal upwelling. Figure 4 (left) is centered around a particular cold filament (∼0.1°C) that is being sharpened by an approximately confluent horizontal surface flow between neighboring mesoscale eddies. In a nearly straight central sector of the filament, Figure 4 (right) shows local outcropping of cold isotherms within the shallow, late-spring, weakly-stratified, surface boundary layer with a thickness of ≈30 m above the thermocline. Strong, narrow downwelling ($\approx -10^{-3}$ m s^{-1}) occurs in the filament middle. This $w(x, z)$ pattern is very much like the idealized solution (Figure 3, bottom right). The temperature filament also has a ribbon of strong cyclonic vorticity (10^{-3} s^{-1}; not shown) generated in vortex stretch-

ing by $\partial_z w$ near the surface, analogous to, but stronger than, the cyclonic vorticity generation in frontogenesis [*Capet et al.*, 2008]. The example shown here is among many submesoscale filaments, fronts, and coherent spiral eddies that spontaneously emerge in this simulation.

4. Conclusions

[15] We present the theory for a new dynamical process, *viz*., surface cold filamentary intensification, analogous to frontogenesis but adapted to a different flow configuration. Horizontal deformation flow acts on a favorably-aligned filamentary temperature extremum to shrink its horizontal scale and generate a double-cell ageostrophic circulation with strong surface convergence and central downwelling that accelerates the intensification rate (compared to SQG). This process provides a hypothesis for explaining the prevalent submesoscale lines in reflectance images. However, the predicted correlation between cold surface filaments and high surfactant concentrations has yet to be tested with measurements, and it is an open question how much convergence lines remain dynamically influenced by rotation when their width becomes very small. Since we have considered here only individual filaments, we have as yet no simple explanation for the submesoscale line separation distance.

[16] Filamentary intensification is yet another mechanism for energizing the oceanic submesoscale regime in conjunction with other mechanisms like mixed-layer instability, frontogenesis, and coherent vortex formation. It effects transfer of available potential energy to smaller scales, kinetic energy generation, surface-layer density restratification, vertical material fluxes, and a route to microscale dissipation. It may also be unstable — as is frontogenesis [*McWilliams et al.*, 2009] — to three-dimensional fluctuations on even smaller scales.

[17] **Acknowledgments.** We appreciate discussions with Ben Holt on reflectance images and sponsorship by ONR (N00014-08-1-0597) and NSF (OCE-0550227, -0612100).

References

Capet, X., J. C. McWilliams, M. J. Molemaker, and A. Shchepetkin (2008), Mesoscale to submesoscale transition in the California Current System: Frontal processes, *J. Phys. Oceanogr.*, *38*, 44–64.

Castelao, R. M., T. P. Mavor, J. A. Barth, and L. C. Breaker (2006), Sea surface temperature fronts in the California Current System from geostationary satellite observations, *J. Geophys. Res.*, *111*, C09026, doi:10.1029/2006JC003541.

Colas, F., X. Capet, J. C. McWilliams, and A. Shchepetkin (2008), 1997–98 El Niño off Peru: A numerical study, *Prog. Oceanogr.*, *79*, 138–155.

Espedal, H. A., O. M. Johannessen, J. A. Johannessen, E. Dano, D. R. Lyzenga, and J. C. Knulst (1998), COASTWATCH'95: ERS 1/2 SAR detection of natural film on the ocean surface, *J. Geophys. Res.*, *103*, 24,969–24,982.

Hakim, G. J., C. Snyder, and D. J. Muraki (2002), A new surface model for cyclone-anticyclone asymmetry, *J. Atmos. Sci.*, *59*, 2405–2420.

Hoskins, B. J. (1982), The mathematical theory of frontogenesis, *Annu. Rev. Fluid Mech.*, *1*, 131–151.

Lapeyre, G., and P. Klein (2006), Impact of the small-scale elongated filaments on the oceanic vertical pump, *J. Marine Res.*, *64*, 835–851.

Leibovich, S. (1983), The form and dynamics of Langmuir circulations, *Annu. Rev. Fluid Mech.*, *15*, 391–427.

McWilliams, J. C., M. J. Molemaker, and E. I. Olafsdottir (2009), Linear fluctuation growth during frontogenesis, *J. Phys. Oceanogr.*, in press.

Zhao, Z., V. Klemas, Q. Zheng, and X.-H. Yan (2004), Remote sensing evidence for baroclinic tide origin of internal solitary waves in the northeastern South China Sea, *Geophys. Res. Lett.*, *31*, L06302, doi:10.1029/2003GL019077.

F. Colas, J. C. McWilliams, and M. J. Molemaker, Institute of Geophysics and Planetary Physics, University of California, Los Angeles, CA 90095-1567, USA. (jcm@atmos.ucla.edu)